Available online at www.sciencedirect.com

ScienceDirect

Physics Procedia 69 (2015) 516 – 523

Physics Procedia

10th World Conference on Neutron Radiography 5-10 October 2014

Quantification of water content across a cement-clay interface using high resolution neutron radiography

Shafizadeh A.[a]*, Gimmi T.[a,c], Van Loon L.[a], Kaestner A.[b], Lehmann E.[b], Maeder U.K.[c] and Churakov S.V.[a]

[a] *Laboratory for Waste Management, Paul Scherrer Institute, 5232 Villigen PSI, Switzerland*
[b] *Neutron Imaging and Activation Group, Paul Scherrer Institute, 5232 Villigen PSI, Switzerland*
[c] *Rock-Water Interaction, Institute of Geological Sciences, University of Bern, 3012 Bern, Switzerland*

Abstract

In many designs for radioactive waste repositories, cement and clay will come into direct contact. The geochemical contrast between cement and clay will lead to mass fluxes across the interface, which consequently results in alteration of structural and transport properties of both materials that may affect the performance of the multi-barrier system. We present an experimental approach to study cement-clay interactions with a cell to accommodate small samples of cement and clay. The cell design allows both in situ measurement of water content across the sample using neutron radiography and measurement of transport parameters using through-diffusion tracer experiments. The aim of the high-resolution neutron radiography experiments was to monitor changes in water content (porosity) and their spatial extent. Neutron radiographs of several evolving cement-clay interfaces delivered quantitative data which allow resolving local water contents within the sample domain. In the present work we explored the uncertainties of the derived water contents with regard to various input parameters and with regard to the applied image correction procedures. Temporal variation of measurement conditions created absolute uncertainty of the water content in the order of ±0.1 (m^3/m^3), which could not be fully accounted for by correction procedures. Smaller relative changes in water content between two images can be derived by specific calibrations to two sample regions with different, invariant water contents.

Selection and peer-review under responsibility of Paul Scherrer Institut

Keywords: Neutron Radiography; Cement; Clay; Cement-Clay Interface; Porosity;

1. Introduction

In the Swiss concept for multiple-barrier nuclear waste repositories, cement and concrete materials will be in contact with clay-rich host rocks (Nagra 2002). Differences in the chemical composition of the pore water of these materials lead to mass flux across the interface, which consequently results in alteration of mineralogical/structural and transport properties of both materials. The mineral alterations and their effect on the pore structure, as well as on transport parameters need to be experimentally studied, and the relevant processes have to be implemented into reactive transport simulations aimed at assessing the repository's safety. Several numerical simulations, laboratory and in-situ experiments and natural analogues provided valuable information regarding possible alterations. The expected reactions at the interface are summarized by Gaucher and Blanc (2006) as follows: A modification of the adsorbed cation populations, dissolution of clay minerals, dissolution of

* Corresponding author. Tel.: +41 56 310 4114; fax: +41 56 310 2821.
E-mail address: amir.shafizadeh@psi.ch

Selection and peer-review under responsibility of Paul Scherrer Institut
doi:10.1016/j.phpro.2015.07.073

portlandite and of accessory minerals and finally precipitation of newly formed minerals in certain regions, with the possibility of an increase in the porosity of the cement and a reduction in the porosity of the clay at the interface (Gaboreau et al., 2011, Traber and Maeder, 2012, Kosakowski and Berner, 2013). Our experimental work intends to provide laboratory observations of the temporal and spatial extent of these processes, and notably of porosity changes. The expected changes are small and of limited extent. It is therefore important to develop suitable investigation techniques. Neutron imaging is a method that is highly sensitive to the water content of a sample and provides well-suited spatial resolution (μm range). Furthermore, it is non-destructive, which allows investigating samples repeatedly at different times. Here we explore the possibilities of neutron imaging to study porosity changes in a quantitative way at a cement-clay interface.

2. Materials and methods

2.1. Samples

We brought a sulphate-resistant Portland cement (Type CEM I 52.5 N HTS, Lafarge, France) into contact with compacted sodium montmorillonite clay. The cement sample was prepared about 14 years ago with a high water to cement ratio of 1.3 using a method developed at the Paul Scherrer Institute (Doehring et al., 1994). Smaller plugs of the desired diameter were cored out of bigger plugs by using a diamond bit. The plugs were then shaped by using sand paper to reach the desired length. The clay sample was obtained from Milos (Greece). All the exchangeable cations of the clay were replaced by sodium to form a homo-ionic Na-montmorillonite (Glaus et al., 2010). Slightly wetted clay powder was compacted to the desired density and geometry in a compaction cell. Table 1 summarizes the properties of both materials, prior to be brought into contact.

Table 1. Description of the samples used in this study (Doehring et al., 1994 and Glaus et al., 2010)

	Geometry (mm)	Porosity (m^3/ m^3)	Pore water pH	Dry bulk density (g/cm^3)	Type
Cement	L=5, D=5	0.63	13.3	0.77	CEM I 52.5 N HTS
Clay	L=5, D=5	0.39	8.7[a]	1.74	Na-montmorillonite

[a] Calculated by GEMS, a geochemical speciation code

The chemical compositions of the cement measured by X-ray fluorescence (XRF) and of the clay measured by inductively coupled plasma atomic emission spectroscopy (ICP-AES) after acid digestion are summarized in Table 2.

Table 2. Chemical composition (g/100 g) of the cement and clay used in this study (Lothenbach and Wieland, 2006 and Glaus et al., 2010)

	SiO_2	Al_2O_3	Fe_2O_3	MnO	MgO	CaO	Na_2O	K_2O	TiO_2	P_2O_5	LOI	SrO	BaO	Li_2O	Rb_2O	CaO (free)	CO_2	SO_3
CEM I 52.5 N HTS[a]	22.3	2.7	1.9	-	0.85	65.7	0.13 (0.04[b])	0.22 (0.08[b])	-	-	-	0.16	0.002	0.03	<0.001	0.45	1.6	2.2
Montmorillonite (Milos)	62.5	20.4	1.94	0.01	3.72	0.02	2.96	0.22	0.16	<0.015	8.81	-	-	-	-	-	-	-

[a]Blaine surface area: 354 m^2/kg
[b]Readily soluble alkalis; they were calculated from the concentrations of alkalis measured in the solution after 5 min agitation at a w/c of 10; present as alkali sulphates.

2.2. Experimental cell

Interface samples with cement (No. 1 in Fig. 1) and clay (No. 2) were placed into a polytetrafluoroethylene (PTFE) cylindrical holder (No. 4) and supported mechanically against the high swelling pressure of the clay in an aluminum chamber (No. 7). Both PTFE and aluminum parts have low neutron attenuation properties which allow receiving better signal from the water present in the sample domain. The cell has two reservoirs within the polyether ether ketone (PEEK) screw caps to keep the cement and clay in contact with their equivalent pore solutions (No. 6). Fluoroelastomer (FKM) O-rings (No. 3) were used to ensure solution reservoirs are sealed. Circulation of cement pore water (pH=13.3) and clay pore water (0.3M NaCl) is possible via outlet channels (not visible in 2D profile). PEEK frits (No. 5) and PEEK screw caps are used to keep the samples in place, especially the swelling clay plug.

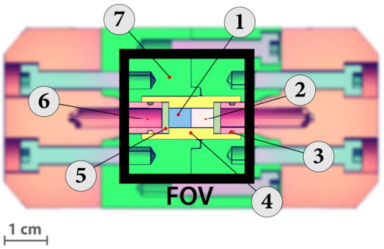

Fig. 1. Cross section view of a sample cell: (1) Cement sample, (2) clay sample, (3) O-rings, (4) PTFE sample holder, (5) PEEK frits, (6) solution reservoirs within PEEK caps, (7) aluminium holder. The framed part in black represents the part exposed to neutrons.

2.3. Neutron radiography measurements

Due to the high sensitivity of neutrons to small amounts of water, neutron radiography was employed as a non-destructive imaging technique to observe water content changes in the sample. Water content can be used as a proxy variable for porosity under the saturated conditions of the experiments. Measurements were carried out at the ICON beamline for imaging with cold neutrons (Kaestner et al., 2011) at the Swiss spallation neutron source (SINQ) of the Paul Scherrer Institute. Neutrons, generated at a spallation source, fly through a collimator and evacuated flight tubes to the sample. A Gadox scintillator is used to convert the transmitted neutrons to light which is recorded then by a CCD camera system and stored digitally as a grey value matrix.

To achieve maximum resolution and sharpness, the smallest possible field of view and the shortest sample-to-detector distance was selected. The experimental parameters used in this study are listed in Table 3.

Table 3. Setup parameters used for the neutron imaging measurements at ICON.

Mean Energy (meV)	Mean Flux (neutrons cm^{-2} s^{-1} mA^{-1})	Aperture (mm)	Collimation Ratio L/D	Resolution (μm)	Field of View (mm)	CCD size (pixel)	Exposure Time (s)	Scintillator
8.53	1.3×10^{7}	20	343	20.3	27.5×27.5	2048×2048	90	Gd (10 and 20 μm)

2.4. Scattering effects

To minimize unsharpness and enhance resolution of the measurements, vital for quantification of porosity alterations, the samples were kept as close as possible to the detector. This small sample-to-detector distance will increase the probability of scattered neutrons to reach the detector, especially during measurement of materials with high scattering cross section. This contribution will lead to underestimation of water contents obtained from the radiographs. To account for these scattering effects, different computational and experimental approaches have been used. Hassanein et al. (2005) and Kardjilov et al. (2005) used Monte Carlo simulations of Point Scattered Function (PScF) to correct the scattering effect in the radiography images. Lehmann et al. (2004) and Kang et al. (2013) showed that deviations of the attenuation function from the exponential law occurred for water layers larger than 2 mm, which suggests constraining water contents in this range if possible. We used these findings in our sample cell design, which limits the water thickness approximately to this range to minimize the scattering effects. In addition, since any of these approaches will not fully account for all the effects recorded in the images (e.g. scattering, beam hardening, slightly variable sample-to-detector distances), an empirical relation for the attenuation coefficient of water from calibration measurements was tested and then used in deriving water contents from the radiographs.

2.5. Image processing procedure

The obtained images $I(E,x,y,t)$ were geometrically aligned, and white spots due to γ-radiation were filtered out by a 2D median filter which also cancels out possible black spots due to pixel failures. The images were then corrected for dark current $I_{dc}(E,x,y,t)$. Since we did not record neutron energy (E) fluctuations, we leave it out here and also position (x,y) is shown as vector $\boldsymbol{x}$. Therefore, $I(\boldsymbol{x},t)$ represents $I(E,x,y,t)$ in the following equations. According to the Beer-Lambert law

$$I(\mathbf{x},t) = I_0(\mathbf{x},t)\exp(-\mu_c d_c - \mu_s d_s - \mu_w d_w) = I_0(\mathbf{x},t)\, r_s(\mathbf{x},t)\,, \tag{1}$$

with $I_0(\boldsymbol{x},t)$ the intensity of the incoming beam, $r_s(\boldsymbol{x},t) = exp(-\mu_c d_c-\mu_s d_s-\mu_w d_w)$ the relative local fluctuations (the fluctuation field) caused by the sample, μ_c, μ_s and μ_w the attenuation coefficients of the cell, the sample (cement or clay) and the pore water,

respectively, and d_c, d_s and d_w the equivalent thicknesses of these layers. The incoming (detected) intensity $I_0(\mathbf{x},t)$ is a function of the position vector $\mathbf{x}$ because of inhomogeneities of the neutron flux and inhomogeneities in the detector system. $I_0(\mathbf{x},t)$ can be written as

$$I_0(\mathbf{x},t) = \overline{I_0}(t)\, r_h(\mathbf{x},t)\,, \tag{2}$$

where $\overline{I_0}(t)$ is the average value of the incoming beam and $r_h(\mathbf{x},t)$denotes the relative local fluctuations due to beam inhomogeneity and detector response. Thus, the $I(\mathbf{x},t)$ image can be written as

$$I(\mathbf{x},t) = \overline{I_0}(t)\, r_h(\mathbf{x},t)\, r_s(\mathbf{x},t)\,. \tag{3}$$

In order to derive the relative sample signal, $r_s(\mathbf{x},t) = exp(-\mu_c d_c - \mu_s d_s - \mu_w d_w)$ (and, finally, the water content of the sample), $I_0(\mathbf{x},t)$ is estimated by an 'open beam' image, $I_{ob}(\mathbf{x},t)$. The open beam image can also be written as

$$I_{ob}(\mathbf{x},t_{ob}) = \overline{I_0}(t_{ob})\, r_h(\mathbf{x},t_{ob})\,. \tag{4}$$

This open beam image necessarily has to be taken before or after the image of the sample, that is, at time t_{ob} and not at time t of the sample image. The transmission image T is

$$T(\mathbf{x},t) = \frac{I(\mathbf{x},t)}{I_{ob}(\mathbf{x},t_{ob})}\,. \tag{5}$$

Thus, we have

$$T(\mathbf{x},t) = \frac{\overline{I_0}(t)}{\overline{I_0}(t_{ob})}\,\frac{r_h(\mathbf{x},t)}{r_h(\mathbf{x},t_{ob})}\, r_s(\mathbf{x},t) = a(t)\, b(\mathbf{x},t)\, r_s(\mathbf{x},t)\,, \tag{6}$$

where $a(t)$ is a scalar dose correction term arising from the different mean intensities of I and I_{ob}, and $b(\mathbf{x},t)$ a term arising from the possibly different local fluctuations between the two images (the dependence of T on $\mathbf{x}$ and t will not be explicitly noted anymore from now on). Both terms are generally different from unity. If the open beam image is taken with the same setup as the image $I(\mathbf{x},t)$ then the heterogeneity term $b(\mathbf{x},t)$ is probably very close to unity, but the intensity term $a(t)$ is unknown. The correct $r_s(\mathbf{x},t)$ and thus the correct water contents can only be obtained by a direct calibration, that is, by a linear scaling of the mean intensity by a factor that should match $1/a(t)$.

To obtain the water content field, the sample image is normalized by an image of the dry sample in the sample holder (which may have to be synthesized from separate images with a dry cement and a dry clay). This reference image, when normalized by an open beam image, is

$$T_{dry} = \frac{\overline{I_0}(t_{dry})}{\overline{I_{ob}}(t_{ob,dry})}\,\frac{r_h(\mathbf{x},t_{dry})}{r_h(\mathbf{x},t_{ob,dry})}\, r_{dry}(\mathbf{x},t_{dry}) = a(t_{dry})\, b(\mathbf{x},t_{dry})\, r_{dry}(\mathbf{x},t_{dry})\,, \tag{7}$$

where $r_{dry}(\mathbf{x},t_{dry})$ is the relative fluctuation field of the dry sample measured at time t_{dry}. The sample transmission T at a given time normalized by T_{dry} is thus

$$\frac{T}{T_{dry}} = \frac{\overline{I_0}(t)}{\overline{I_0}(t_{dry})}\,\frac{\overline{I_{ob}}(t_{ob,dry})}{\overline{I_{ob}}(t_{ob})}\,\frac{r_h(\mathbf{x},t)}{r_h(\mathbf{x},t_{dry})}\,\frac{r_h(\mathbf{x},t_{ob,dry})}{r_h(\mathbf{x},t_{ob})}\,\frac{r_s(\mathbf{x},t)}{r_{dry}(\mathbf{x},t_{dry})}\,, \tag{8}$$

or, when expressed with terms a and b for the mean intensities and the fluctuations and with $r_w(\mathbf{x},t) = exp(-\mu_w d_w)$,

$$\frac{T}{T_{dry}} = \frac{a(t)}{a(t_{dry})}\,\frac{b(\mathbf{x},t)}{b(\mathbf{x},t_{dry})}\, r_w(\mathbf{x},t) = a'(t)\, b'(\mathbf{x},t)\, r_w(\mathbf{x},t)\,. \tag{9}$$

Here, $a'(t)$ is the term arising from the different mean intensities of the sample image at time t, the image of the dry sample at time t_{dry}, and the open beam images at times t_{ob} and $t_{ob,dry}$. Very likely, this term will in most cases be different from 1 for each

sample image taken at time *t*. The term *b'(t)* arises from the local heterogeneities which may be different at different times *t*, t_{dry}, t_{ob}, and $t_{ob,dry}$. As stated above, if the open beam images are taken with the same setup as the sample image or the image of the dry sample, respectively, the corresponding *b* values and also *b'* may be about *1*. Accordingly, we may write

$$\frac{T}{T_{dry}} \approx a'(t)\, r_w(\mathbf{x},t) = a'(t)\exp(-\mu_w d_w(\mathbf{x},t)). \tag{10}$$

The water content field of a sample is obtained from the total thickness d_T of the sample and the thickness of the water phase d_w as

$$\theta(\mathbf{x},t) = \frac{d_w(\mathbf{x},t)}{d_T(\mathbf{x},t)} = \frac{1}{\mu_w\, d_T(\mathbf{x},t)} \ln\left(\frac{T_{dry}}{T}\, a'(t)\right). \tag{11}$$

Let us assume that the first image in a series of sample images is calibrated such that the correct water content is obtained. Then, we have $a'(t_1) = 1$. The following images *i=2, 3, ...* can then be normalized to this first image of the series by a dose window correction, that is, by using a region with supposedly constant scattering properties as an internal standard. The dose window corrections for images *i=2, 3, ...* are done according to

$$\frac{T_i}{T_{dry}} \approx a'(t_i)\frac{dw_1}{dw_i}\, r_w(\mathbf{x},t), \tag{12}$$

where dw_1 is the mean value of the dose window (internal standard) in the calibrated image 1 and dw_i the mean value of the internal standard in image *i*. After applying this correction, the value of the dose window in each image *i* will be equal to the value in the calibrated image *1*, from which correct water contents are obtained.

Average water contents of the sample at different positions along the cylinder axis were finally calculated by an appropriate weighting of the local water contents perpendicular to the axis.

3. Results

To measure the macroscopic scattering cross section of water (μ_w) a separate calibration measurement with known water thicknesses, at the same sample-to-detector distance as the measurements, was performed. Fig. 2 shows the calibration cell and its transmission values over the specified profile. Using Eq. 11 the water thickness was calculated and plotted versus the true water thickness known from the cell geometry. It can be seen that a fixed value of μ_w will cause deviation between the calculated and the true water thickness of the cell, caused mainly by the contribution of scattered neutrons and beam hardening in the recorded radiograph. Therefore, an empirical relation between the scattering cross section of water and the true thicknesses of water $\mu_w = \mu + \beta d_w$ was implemented (Hussey et al., 2012) and values of $\mu = 4.0$ cm^{-1} and $\beta = -1.8$ cm^{-2} were estimated to give the best correction for the water content calculations (Fig. 2d). This empirical dependency of μ_w on the water thickness will modify Eq. 11 to

$$\theta(\mathbf{x},t) = \frac{d_w(\mathbf{x},t)}{d_T(\mathbf{x},t)} = \frac{1}{[\mu + \beta\, d_w(\mathbf{x},t)]\, d_T(\mathbf{x},t)} \ln\left(\frac{T_{dry}}{T}\, a'(t)\right), \tag{13}$$

and by solving it for d_w we obtain

$$\theta(\mathbf{x},t) = \frac{d_w(\mathbf{x},t)}{d_T(\mathbf{x},t)} = -\frac{1}{d_T(\mathbf{x},t)}\left[\frac{\mu}{2\beta} + \sqrt{\left(\frac{\mu}{2\beta}\right)^2 + \frac{1}{\beta}\ln\left(\frac{T_{dry}}{T}\, a'(t)\right)}\right]. \tag{14}$$

This empirical improvement of the calibration function does not account for the spatially slightly variable distance between the sample surface and the detector, caused by the circular geometry of the sample, but nevertheless improves the quantification of the water contents.

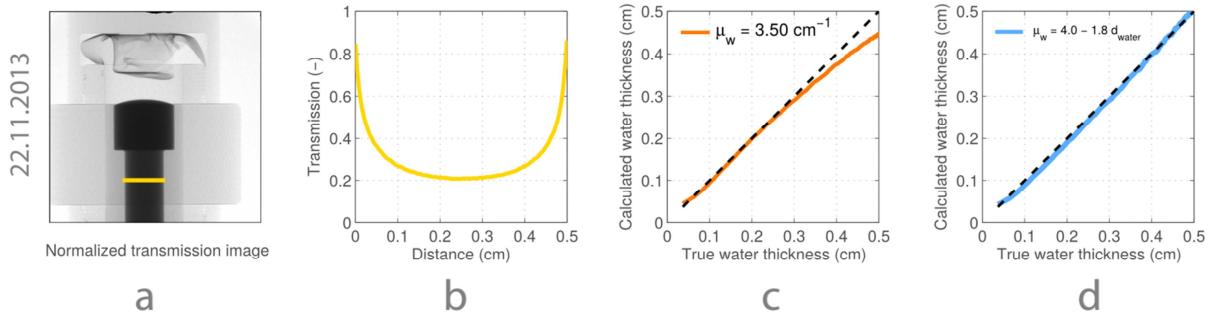

Fig. 2. Transmission images of a cylindrical cell filled with water (a) with its transmission profile (b), its calculated water thickness assuming a fixed, fitted μ_w (c) and calculated water thickness assuming $\mu_w = \mu + \beta d_w$ and the fitted parameters (d)

An image of the assembled sample cell and neutron transmission images of the dry and wet samples are shown in Fig. 3. We did pick ten different dose window regions from the non-reacting part of the sample cell. Numbers 1 to 5 were located in different parts of the PTFE sample sleeve, and numbers 6 to 10 in the aluminum part of the sample holder (Fig. 4a). As can be seen from Fig. 4b, the derived water contents for the image at t = 64 days (using best fit parameters obtained from the first calibration measurement) are roughly in the correct range (see Table 1, 0.63 for the cement and 0.39 for the clay), irrespective of the used dose window. Therefore, we decided to use generally dose window number 8 which provides the closest value to our known 0.63 porosity of the cement.

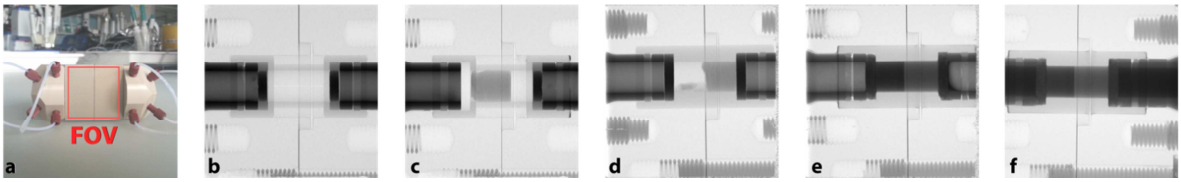

Fig. 3. Image of the sample cell with the neutron field of view (FOV) shown as red square (a) together with transmission neutron radiographs of an empty cell (b), a dry cement on the left (c), a dry clay on the right (d), a cement-clay interface at time d = 64 days (e) and the same interface at time d = 104 days (f). The neutron transmission images shown are corrected, but not geometrically aligned yet.

While the calibrated parameters give water contents in the expected range for both cement and clay at time t = 64 days, water contents of the sample at time t=104 days are underestimated (Fig. 4c). To investigate possible sources of this deviation, we performed a second calibration measurement (Fig. 5) and observed similar underestimation of water contents of the second calibration (the blue line in Fig. 5d) by using the fitted parameters from the first calibration. The reason for these deviations is not clear at present and could be related to (a) possible temporal variations of the energy spectrum of the beam, (b) changes in the beamline settings (e.g. different beam limiter areas) or (c) different sample-to-detector distances caused by the sample's cylindrical geometry which could be magnified when both calibration cells were placed not exactly at the same distance to the detector but only as close as possible (2-4 mm).

In order to match the correct water contents in the second calibration, new parameters (μ = 3.9 cm^{-1} and β = -2.6 cm^{-2}) should be used (the green line in Fig. 5d). This implies that no specific calibration can provide parameters that are equally suited for all sample images taken at different times. However, a two-parameter calibration seems always suited. This suggests that for an improved measurement of sample water contents at each time, two internal parts of the sample with known water contents should be used in Eq. 14 to obtain the best-fit parameters, and the fitted parameters should then be used to calculate the water content in the rest of the sample domain.

From our sensitivity analysis (Fig 4d), we estimated the absolute uncertainty of the obtained water contents to be around ±0.1 (m^3/m^3) using either of the two calibration series. Corrected images are shown in Fig. 6. It can be observed in each image that the cement (left) has much higher water content than the clay (right). In addition, slightly increased water contents close to the interface on the cement side (R1 in Fig. 6) and decreased water contents on the clays side (R2 in Fig. 6) were observed after several months of interaction. Further studies are necessary, though, including an improved quantification of the water contents, before these findings can be interpreted in terms of possible mineralogical changes.

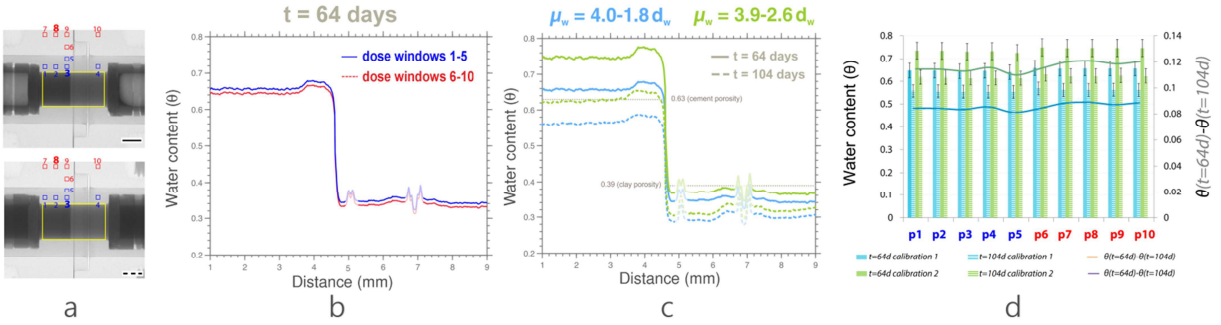

Fig. 4. Corrected images at t = 64 days (top) and at t = 104 days (bottom); cement is located on the left, clay on the right side of the sample (a). Calculated water content at t = 64 days based on two different dose window sets, blue squares number 1-5 in the PTFE and red squares number 6-10 in the aluminium. The water content profile is obtained as a weighted average (weights according to the local thickness of the cylindrical sample) over the yellow rectangular selection. The x-axis represents the horizontal distance through the sample and the y-axis the vertically averaged water contents (b). Water content profiles of the interface at t = 64 days and t = 104 days, using one fixed dose window (red square number 8 in both a- top and a-bottom). Blue lines are calculated using parameters obtained from first calibration cell and the green line corresponds to the parameters obtained from the second calibration (c). Calculated water contents from all ten dose window regions, using both calibration parameters, for both t = 64 days and t = 104 days, and their absolute difference from one time to another (d).

4. Discussion

Errors in water contents derived as outlined above may originate from several reasons.

- Use of the Beer-Lambert law
  The Beer-Lambert law is only an approximation of the true attenuation effects. Errors originating from the application of the Beer-Lambert may be due to scattering effects that depend on both, the thickness of the water layer and the distance of the sample to the detector. A detailed quantification of these effects for our cylindrical samples, for instance by Point Scattered Functions, is very difficult.
- Neglect of $b(\boldsymbol{x},t)$ and $b'(\boldsymbol{x},t)$
  A linear calibration of a single image and linear scaling of further images to be compared with the single image is only possible if the factors $b(\boldsymbol{x},t)$ and $b'(\boldsymbol{x},t)$, respectively, are about unity. The effect of neglecting these factors may be estimated from comparison of repeated open beam images, i.e., by calculating $r_h(\boldsymbol{x},t_{ob,1}) / r_h(\boldsymbol{x},t_{ob,2})$ obtained at different times. It may then also be concluded whether this leads mostly to a random effect in $\boldsymbol{x}$, which averages out, or whether it may lead to trends within an image.
- Calibration value of μ_w
  So far, the μ_w values were obtained empirically by a calibration of a water sample at a certain time. The value of μ_w depends on the energy spectrum of the neutrons at the measurement time. If the energy spectrum varies with time, this may also contribute to the error of the water content at very small sample to the detector distances. Also, the two parameters that affect the contribution of scattered neutrons, beam hardening, the water thickness and the distance of the sample to the detector, were correlated in the calibration image, but uncorrelated in the sample image. Thus, the obtained calibration function cannot be considered as universal for all sample regions.

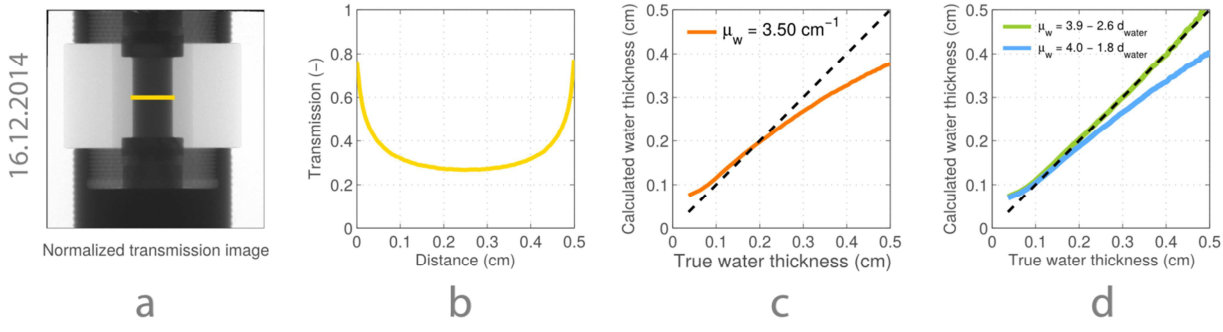

Fig. 5. Transmission image of the second cylindrical calibration cell filled with water (a) with its transmission profile (b), its calculated water thickness assuming a fixed μ_w (c) and calculated water thickness assuming $\mu_w = \mu + \beta d_w$ and the fitted parameters (d) at a different time. The fitted parameters from the first calibration series (Fig. 2d) (the blue line) are underestimating the water thicknesses of the cell, indicating temporal variation of the effective $\mu_w = \mu + \beta d_w$.

5. Summary and Conclusion

In this paper we presented a methodology to study the water distribution profile across an evolving cement-clay interface, using the neutron radiography technique. The technique delivered quantitative data which allowed resolving local water contents across the interface, with absolute uncertainties in the order of ±0.1 (m^3/m^3) by using parameters obtained from a reference calibration cell. Improved water contents were derived by specific calibrations to two sample regions of the sample with invariant water contents. Several interface samples have been prepared to verify the reproducibility of the results and to benefit from the working methodology by investigating a larger number of cement-clay interface samples.

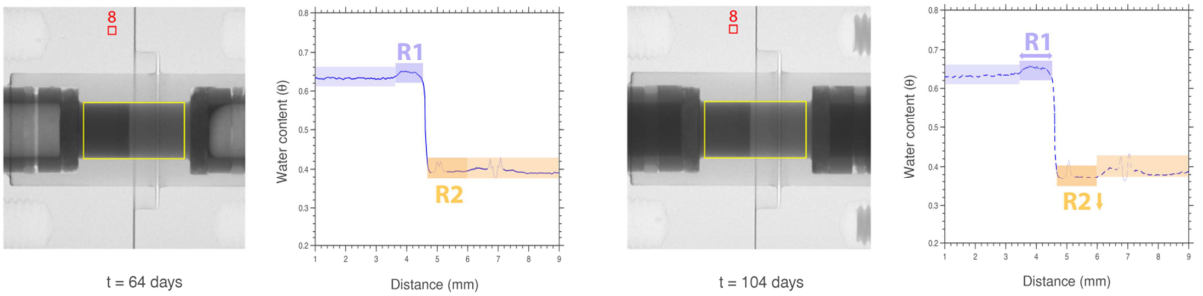

Fig. 6. Corrected neutron radiographs of one cement-clay interface at t = 64 days and t = 104 days and their corrected water content profiles (averages along the horizontal of the yellow rectangular selection, cement is located left, clay right). The red square represents the part of the image selected for dose window correction. The parameters used in water content calculations (Eq. 14) were obtained from specific calibration using two internal parts of the sample with known water contents (0.63 for cement at 1mm and 0.39 for clay at 9mm, far away from the interface. Small peaks on the water content profiles are due to the sample cell geometry and not to changes within a sample.

Acknowledgements

We appreciate kind support from Erich Wieland and Dominik Kunz for providing the cement plugs, Martin Glaus and Sabrina Frick for providing the clay samples and Harald Siebold for assisting in the design of the sample cell. Financial support by the Swiss National Cooperative for the Disposal of Radioactive Waste (NAGRA) is kindly acknowledged.

References

Döhring, L., Görlich, W., Rüttener, S., Schwerzmann, R., 1994. Herstellung von homogenen Zementsteinen mit hoher hydraulischer Leitfähigkeit. Nagra unpublished report, Wettingen, Switzerland.

Gaboreau, S., Prêt, D., Tinseau, E., Claret, F., Pellegrini, D., & Stammose, D. (2011). 15 years of in situ cement–argillite interaction from Tournemire URL: Characterisation of the multi-scale spatial heterogeneities of pore space evolution. Applied Geochemistry, 26(12), 2159-2171.

Gaucher, E.C., Blanc, P., 2006. Cement/clay interactions – a review: experiments, natural analogues, and modeling. Waste Manage. 26 (7), 776–788.

Glaus, M. A., Frick, S., Rossé, R., & Van Loon, L. R. (2010). Comparative study of tracer diffusion of HTO, 22Na+ and 36Cl− in compacted kaolinite, illite and montmorillonite. Geochimica et Cosmochimica Acta, 74(7), 1999-2010.

Hassanein, R., Lehmann, E., & Vontobel, P. (2005). Methods of scattering corrections for quantitative neutron radiography. Nuclear Instruments and Methods in Physics Research Section A: Accelerators, Spectrometers, Detectors and Associated Equipment, 542(1), 353-360.

Hussey, D. S., Spernjak, D., Weber, A. Z., Mukundan, R., Fairweather, J., Brosha, E. L., ... & Borup, R. L. (2012). Accurate measurement of the through-plane water content of proton-exchange membranes using neutron radiography. Journal of Applied Physics, 112(10), 104906.

Kaestner, A. P., Hartmann, S., Kühne, G., Frei, G., Grünzweig, C., Josic, L., Schmid, F., & Lehmann, E. H. (2011). The ICON beamline–a facility for cold neutron imaging at SINQ. Nuclear Instruments and Methods in Physics Research Section A: Accelerators, Spectrometers, Detectors and Associated Equipment, 659(1), 387-393.

Kang, M., Bilheux, H. Z., Voisin, S., Cheng, C. L., Perfect, E., Horita, J., & Warren, J. M. (2013). Water calibration measurements for neutron radiography: application to water content quantification in porous media. Nuclear Instruments and Methods in Physics Research Section A: Accelerators, Spectrometers, Detectors and Associated Equipment, 708, 24-31.

Kosakowski, G., & Berner, U. (2013). The evolution of clay rock/cement interfaces in a cementitious repository for low-and intermediate level radioactive waste. Physics and Chemistry of the Earth, Parts A/B/C, 64, 65-86.

Lehmann, E. H., Vontobel, P., & Kardjilov, N. (2004). Hydrogen distribution measurements by neutrons. Applied Radiation and Isotopes, 61(4), 503-509.

Lothenbach, B., & Wieland, E. (2006). A thermodynamic approach to the hydration of sulphate-resisting Portland cement. Waste Management, 26(7), 706-719.

Nagra, 2002. Project Opalinus Clay: Models, Codes and Data for Safety Assessment. Demonstration of disposal feasibility for spent fuel, vitrified high-level waste and long-lived intermediate-level waste (Entsorgungsnachweis). Nagra Technical Report NTB 02-06. Nagra, Wettingen, Switzerland.

Traber, D., Mäder, U.K., 2012. Reactive Transport Modelling of the Diffusive Interaction Between Opalinus Clay and Concrete. Nagra Unpublished Report. Nagra, Wettingen, Switzerland.